Low-Temperature Synthesis of Ultra-High-Temperature Coatings of ZrB 2 Using Reactive Multilayers

Low-Temperature Synthesis of Ultra High-Temperature Coatings of ZrB_2 Using Reactive Multilayers

Dongwoo Lee, Gi-Dong Sim, Kechao Xiao, and Joost J. Vlassak*

ABSTRACT

We demonstrate a route to synthesize ultra high-temperature ceramic coatings of ZrB_2 at temperatures below 1,300 K using Zr/B reactive multilayers. Highly textured crystalline ZrB_2 is formed at modest temperatures, because of the absence of any oxide at the interface between Zr and B, and the very short diffusion distance that is inherent to the multilayer geometry. The kinetics of the ZrB_2 formation reaction is analyzed using high-temperature scanning nano-calorimetry, and the microstructural evolution of the multilayer is revealed using transmission electron microscopy. We show that the Zr/B reaction proceeds in two stages: (1) inter-diffusion between the nano-crystalline Zr and the amorphous B layers, forming an amorphous Zr/B alloy; and (2) crystallization of the amorphous alloy to form ZrB_2. Scanning nano-calorimetry measurements performed at heating rates ranging from 3,100 to 10,000 K/s allow determination of the kinetic parameters of the multilayer reaction, yielding activation energies of 0.47 eV and 2.4 eV for Zr/B inter-diffusion and ZrB_2 crystallization, respectively.

Keywords: ZrB_2, UHTC, nano-calorimetry, reaction kinetics, reactive multilayer

School of Engineering and Applied Sciences, Harvard University, Cambridge, Massachusetts 02138, United States

*e-mail: vlassak@seas.harvard.edu, Phone: 617-496-0424, Fax: 617-495-9837

INTRODUCTION

ZrB_2 is an ultra high-temperature ceramic (UHTC) with a unique set of properties, including an extremely high melting point, very high hardness, exceptional resistance to erosion, and excellent thermal and electric conductivity. Due to this combination of properties, ZrB_2 has garnered intense attention as a structural material in extreme environments, such as propulsion systems, leading edges of hypersonic flight vehicles, and heat shields for atmospheric re-entry[1-3]. Practical application of ZrB_2, however, has been impeded because of its poor sinterability. ZrB_2 is conventionally fabricated using hot pressing (HP), spark plasma sintering (SPS), or pressure-less sintering (PS), processes that require very high temperature (> 2,200 K) to achieve dense ZrB_2 structures[2]. Even with applied pressures as high as 40 MPa, formation of pure ZrB_2 requires temperatures in excess of 1,950 K to achieve full density[2, 4]. A great deal of research has been conducted in an attempt to enhance the sinterability of ZrB_2 by refining the particle size of the raw materials and by including additives such as C, SiC, B_4C, WC, B_2O_3 or $MoSi_2$[2, 4-11]. Utilizing these methods, recent studies have demonstrated processing temperatures of dense ZrB_2 as low as 1,750 K in the presence of additives.

Here we demonstrate that it is possible to synthesize crystalline ZrB_2 at temperatures below 1,300 K through use of Zr/B reactive multilayers. As shown schematically in Figure 1a, a reactive multilayer consists of alternating Zr and B layers with a nominal stoichiometry of 1:2. Upon heating, Zr and B react to form ZrB_2 in an exothermic process. We have used nano-calorimetry (Figure 1b and c) combined with transmission

electron microscopy (TEM) to explore the nature of the solid-state reaction and the structural changes that occur in the multilayer. Calorimetry has been used extensively to examine the thermodynamics and kinetics of multilayer reactions[12-20]. Nano-calorimetry sensors can significantly enhance the study of these solid-state reactions because of their extraordinary sensitivity and extremely small thermal mass[21-23]. These features make it possible to perform measurements on very thin multilayers over a much broader range of heating rates than traditional calorimetry, ranging from isothermal to 10^5 K/s[21, 22, 24-31]. Current nano-calorimetry sensor designs allow measurements at temperatures as high as 1,300 K[21].

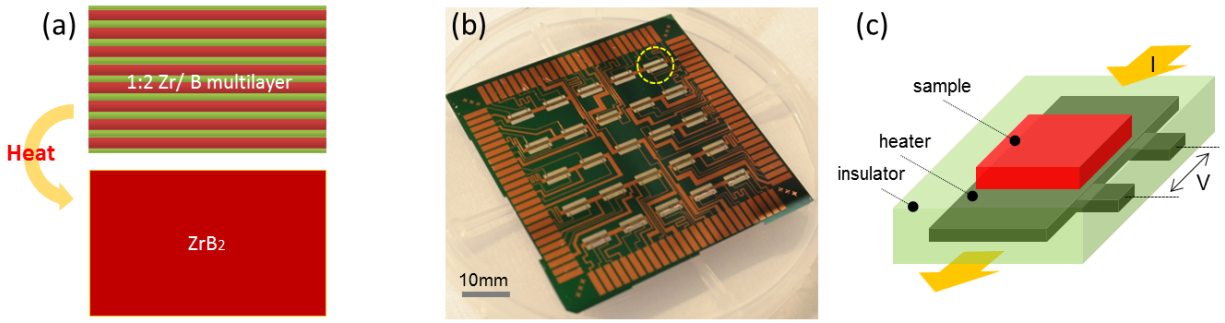

Figure 1. Nano-calorimetry analysis of the Zr/B solid-state reaction: (a) Schematic representation of the cross-section structure of a Zr/B reactive multilayer, before and after reaction. (b) PnSC device with 25 nano-calorimetry sensors. (b) A schematic representation of a nano-calorimetry sensor with a 4-point measurement scheme.

EXPERIMENTAL

Nano-calorimetry sensors

All nano-calorimetry measurements were performed using a parallel nano-scanning calorimeter (PnSC)[25, 32]. This device consists of a 5x5 array of micromachined calorimetry sensors (Figure 1b). Each sensor consists of a thin metal layer that is patterned to serve both as a heating element and a resistance thermometer in a four-point measurement scheme. As illustrated schematically in Figure 1c, this heating element/thermometer is encapsulated in a thin membrane that insulates the heating element from its surroundings. The sample of interest is deposited in the area between the voltage leads as indicated in Figure 1c. To perform a calorimetry scan, an electric current is supplied through the heating element, which results in Joule heating of sample and addendum. The measured current and voltage are used to determine the power supplied to the sensor and the resistance of the heating element, which is calibrated to temperature.

The PnSC device in this study was designed for high-temperature measurements. Specifically, the heating element was fabricated from a 100 nm thick W-Ti alloy film with a high recrystallization temperature[33], extending the operating temperature to 1,400 K. The membrane was fabricated from Si_3N_4 with a total thickness of approximately 300 nm. Figure S1 in Supporting Information provides more detailed information on the micro-fabrication processes used to make the device.

Before depositing the Zr/B multilayer on the nano-calorimetry sensors, the sensors were stabilized and calibrated. The sensors were stabilized by resistively heating them to 1,400 K for 50 thermal cycles, each one of which had a duration of 1.5 sec. These thermal cycles resulted in a small decrease in the room temperature resistance of the heating element because of microstructural changes in the Ti/W alloy. Once the resistance of the heating element was stable, the temperature coefficient of resistance (TCR) of each sensor in the PnSC device was measured by heating the device in an Ar-filled vacuum furnace and by recording the resistance as a function of temperature from 302 K to 452 K in steps of 30 K. High-temperature calibration data was obtained by melting 100 nm Ag samples on select sensors.

Synthesis of reactive multilayers

After calibration of the sensors, Zr/B multilayer samples with bilayer periods of 4.1 and 8.3 nm were deposited onto the sensors of the PnSC device using magnetron sputtering. All samples in this study had a total thickness of 66 nm and the thicknesses of the individual layers comprising the multilayer were chosen to ensure formation of stoichiometric ZrB_2 on completion of the reaction. The multilayers were deposited using an ATC 1800 system (AJA International) with a base pressure of $< 2 \times 10^{-7}$ Torr and an Ar working pressure of 5 mTorr. To ensure uniformity, the substrate holder was rotated at 10 rpm during the deposition process; the temperature of the substrate holder was not controlled. Zr was deposited at a rate of 4.8 nm/min using a 99.99% Zr target (Ø 50.8 mm) and a DC power of 80 W. B was deposited at a rate of 0.2 nm/min using a 99.95% B target (Ø 50.8 mm) and an RF power of 150 W. Immediately before sample deposition, Zr and B were sputtered for one hour to lower impurity levels in the chamber

and to remove any oxide layers from the sputter targets. The multilayer coating was started and terminated with half layers of B, to impose periodic boundary conditions. To prevent oxidation of the samples during the measurements, a 30 nm Si_3N_4 capping layer was sputter deposited (RF 150 W, 4mTorr of Ar) on top of the multilayer, immediately after deposition of the multilayer and without breaking vacuum. All samples were deposited through a micro-fabricated Si shadow mask. The mass of the samples was estimated from the deposition flux and the area of the windows in the shadow mask to be 660±70 ng.

Nano-calorimetry measurement

All nano-calorimetry measurements were performed using a custom-built, low-noise data acquisition system described in detail in Xiao et al[28]. Typical noise levels in the measurements were less than 0.1%. AC measurements were performed at a heating rate of approximately 3,000 K/s and an angular frequency of 3,272.5 rad/s, using AC and DC current components in accordance with the selection criteria in Xiao et al[28]. For the AC measurements, the in-phase and out-of-phase response of the sensor was determined by dividing measured voltage and current signals into segments consisting of an integer number of AC oscillation periods, and applying a discrete Fourier transform (DFT) to every segment as described by Xiao et al[28, 34]. AC measurements were performed on three different multilayer samples to measure the heat capacity, C_p, as a function of temperature, both before and after reaction. DC scanning measurements were performed on other multilayer samples to investigate the kinetics of the solid-state reaction. Measurements were carried out at nominal heating rates of 3,100, 5,200, 7,000, 8,600, and 10,000 K/s. For these measurements, both the

temperature of the sample and the power supplied to it were determined directly from the heating element as described earlier. Each of the DC measurements consisted of three successive scans. The multilayer samples reacted during the first scan and this scan contained the calorimetric signature of the solid-state reaction. The second scan was used to establish a baseline for the first scan. The third scan was performed and compared with the second scan to confirm that the reaction was complete after the first scan. All nano-calorimetry measurements in this study were made in vacuum ($< 1 \times 10^{-6}$ Torr) to minimize any heat loss to the environment. The results from the DC scans were combined with the C_p data from the AC scans to determine the enthalpy released during the multilayer reaction. The data reduction algorithm used to analyze the calorimetric signal of the solid-state reaction and to determine the rate of change of the reaction enthalpy during the reaction are reported in detail in Lee et al[21].

TEM observation

Cross-sectional TEM micrographs and selected area diffraction patterns (SADP) were acquired using a JEOL 2100 system operating at 200 KeV. To prepare the TEM samples, 10 x 2 μm^2 blocks were isolated from the samples of interest using a focused beam of Ga ions (30 keV, 150 pA) inside a Zeiss NVision 40 Dual-Beam system. These blocks were attached to an Omniprobe and further thinned to approximately 100 nm using a 30 KeV, 40 pA Ga ion beam. Finally, Ar ion milling was performed in a Nanomill 1040 operating at 500 eV and 140 pA to ensure electron transparency and to remove any Ga ions introduced by the focused ion beam. To obtain TEM samples at various stages of the multilayer reaction, multilayer samples were taken through the normal calorimetry measurement and quenched upon reaching specific temperatures.

RESULTS AND DISCUSSION

Figure 2a depicts temperature as a function of time for typical DC scans performed on multilayer samples. It is evident that the first temperature scan performed on a sample has a section where the heating rate first increases and then decreases, while the subsequent scan does not. This section starts around 500 K and is the result of exothermic reactions that take place in the samples. Figure 2b presents the heat capacity of a sensor with a multilayer sample and the corresponding addendum, measured using AC scans. The heat capacities of the unreacted and reacted multilayers are essentially indistinguishable and rise slowly with temperature.

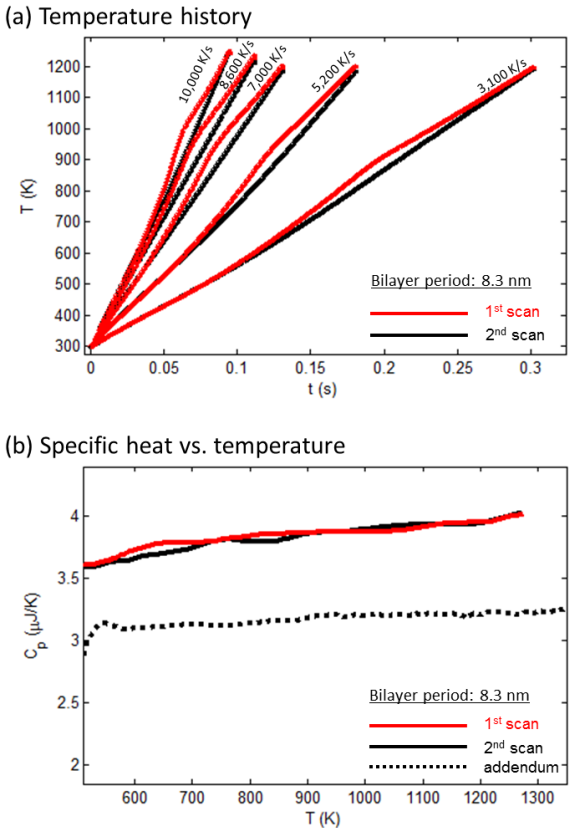

Figure 2. (a) Temperature histories for the Zr/B multilayer samples with a bilayer period of 8.3 nm. (b) Heat capacity of a sensor with a multilayer sample (solid lines) and heat capacity of addendum (dotted line), both obtained from AC measurements.

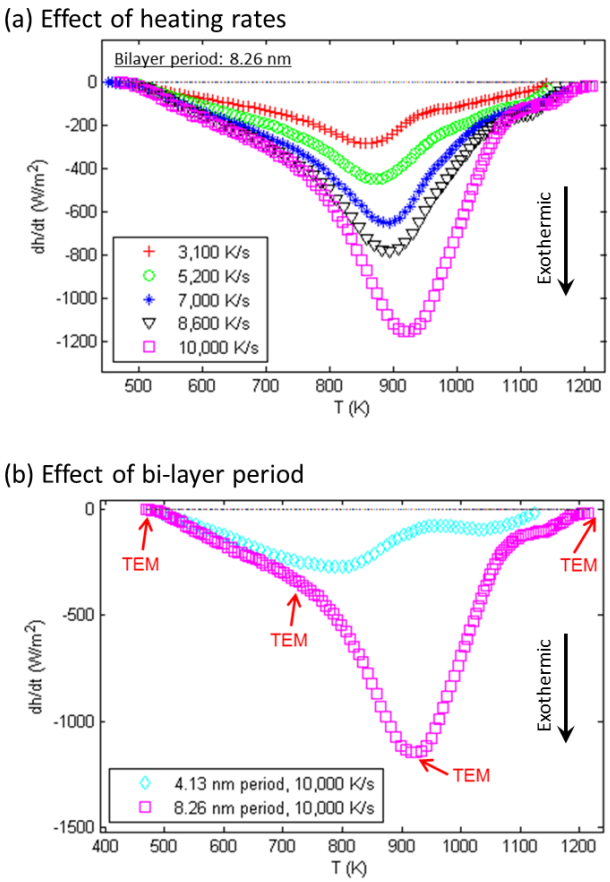

Figure 3. Rate of change of the reaction enthalpy per unit area of Zr/B multilayer: (a) Enthalpy rate per unit area vs. temperature for Zr/B multilayer samples with a bilayer period of 8.3nm. (b) Enthalpy rate per unit area for multilayer samples with two different bilayer periods obtained at a heating rate of 10,000 K/s. The temperatures from which samples were quenched for TEM observations have been marked with arrows.

The temperature histories of the samples can be used to calculate the reaction enthalpy rates produced by the Zr/B reaction. Figure 3 displays the enthalpy rate per unit area as a function of temperature. Figure 3a shows the effect of scan rate, while Figure 3b reveals the effect of the bilayer period of the multilayers. The scans reveal two separate exothermic reactions: a reaction with a strong enthalpy signal and a reaction with a much weaker enthalpy signal at a slightly higher temperature. Figure 3a shows that both peaks shift to higher temperatures as the heating rate increases. Figure 3b clearly demonstrates that the two peaks become more distinct with decreasing bilayer period.

We now show that the first peak corresponds to the amorphization of the Zr/B multilayers as a result of inter-diffusion of B and Zr, while the second peak is associated with the crystallization of the amorphous Zr/B alloy.

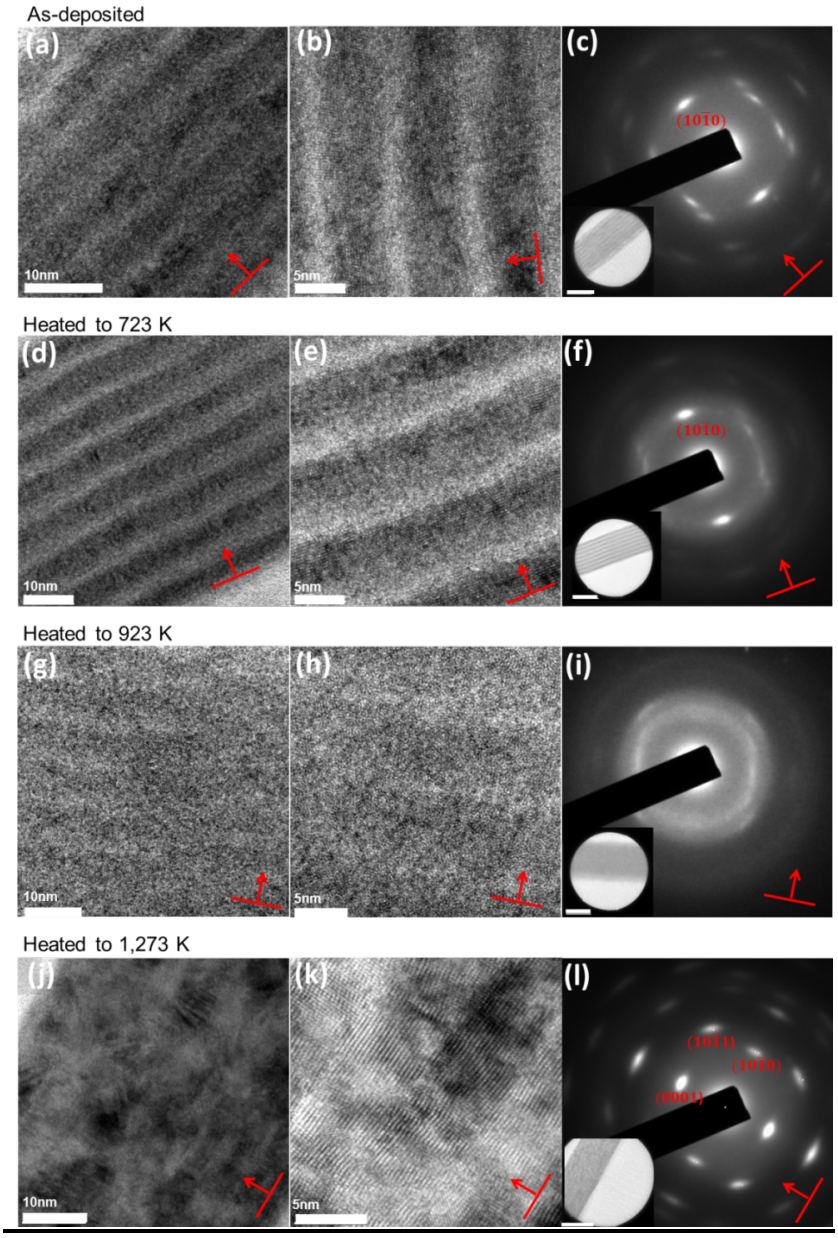

Figure 4. TEM observations on an as-deposited sample (a-c), a sample heated to 723 K (d-f), a sample heated to 923 K (g-i), and a fully reacted sample (j-l): (a,b,d,e,g,h,j,k) Bright-field images are shown for the four different samples. The sample normal are indicated by the arrows. (c,f,i,l) Selected area diffraction patterns obtained from the areas indicated in insets. The scale bars in the insets are 50 nm. All samples had a bilayer period of 8.3 nm and were heated to the relevant temperature at a nominal rate of 10,000 K/s, before being quenched to room temperature.

Figure 4 presents a series of TEM cross-sections that illustrate the reaction sequence. The micrographs were taken on samples that were heated to the temperatures marked by the arrows in Figure 3b, i.e., samples that were heated through different stages of the reaction, before being quenched. The bright-field images in Figures 4a and b clearly show that as-deposited samples have a structure that consists of alternating layers of amorphous B (light) and nano-crystalline Zr (dark). Figure 4c shows an electron diffraction pattern for the as-deposited sample, which indicates that the Zr layers have a (10*10*) crystallographic texture (Powder Diffraction File #050665) and that no other crystalline phases are present. Figures 4d-f and Figures 4g-i show micrographs for samples heated to 723 and 923 K, respectively. It is evident that the Zr and B layers in these samples have inter-diffused and have started to form an amorphous Zr/B alloy. At 723 K, the layered structure of the sample is still present, but the Zr diffraction pattern in Figure 4f is more diffuse, indicative of the onset of amorphization. At 923 K, the peak temperature for the first reaction, the layered structure is mostly gone (Figure 4g, h) and the diffraction pattern is now a diffuse halo (Figure 4i), typical for an amorphous material. A few weak diffraction spots can still be discerned, however, indicating that the amorphization process is not yet complete at this temperature. Figures 4j-l show the results for a sample heated to 1,273 K, well above the temperature at which the second reaction is complete. The change in structure is dramatic: the sample now consists of crystalline ZrB_2 with a (0001) texture (Powder Diffraction File #340423). No other crystalline phases from the Zr-B phase diagram are observed. Evidently the second peak in the enthalpy rate corresponds to the crystallization of the amorphous Zr/B alloy to form the ZrB_2 compound. The ZrB_2 has a (0001) texture, which is somewhat

surprising given that the ZrB_2 alloy is amorphous. The texture is a strong indication that the crystalline phase nucleated at the top or bottom interface of the multilayer coating, or possibly at the original locations of the Zr/B interfaces.

The reaction sequence explains the observation in Figure 3b that the first enthalpy rate peak shifts to a lower temperature with decreasing bilayer period. As the bilayer period decreases, so does the diffusion distance, allowing intermixing of the two phases at lower temperature for a fixed heating rate. Integrating the reaction enthalpy rates in Figure 3 with respect to time provides the formation enthalpy of the ZrB_2 compound. The formation enthalpy measured for the samples with a bilayer period of 8.3 nm is 190 ± 23 kJ/mol, while that for the samples with a bilayer period of 4.1 nm is 74 ± 23 kJ/mol, respectively 64% and 25% of the formation enthalpy of bulk ZrB_2[35, 36]. The TEM micrographs indicate a complete conversion of the multilayer to ZrB_2. Consequently the formation enthalpy deficit can be attributed to intermixing of Zr and B during the deposition process. The enthalpy values are consistent with an intermixed layer of approximately 1.5 nm at each B/Zr interface. Similar intermixing has been observed in other multilayer systems. [13, 14].

The first step in the reaction sequence involves the formation of an amorphous phase caused by the inter-diffusion of B and Zr. As discussed in Supporting Information, the kinetics of this process can be determined from the reaction enthalpy rate curves in Figure 3 using a simple one-dimensional diffusion model. According to this diffusion model, there exists a simple relationship between the enthalpy released in the reaction and the absolute temperature,

$$\ln(H+Ho)\frac{dH}{dt}=2\ln\alpha\Delta H\frac{2D_o}{t_{Zr}}-\frac{E_d}{k_BT}, \quad (1)$$

where H_o is the enthalpy associated with the intermixing, α is a constant defined in Supporting Information, ΔH is the enthalpy of mixing associated with one bilayer period λ, t_{Zr} is the thickness of the Zr layers, k_B is the Boltzmann constant, E_d is the diffusion activation energy, and D_o is the pre-exponential factor of the diffusivity. Figure 5a shows a graph of $\ln(H+Ho)\frac{dH}{dt}$ versus $\frac{1}{k_BT}$ for the temperature range where Zr and B inter-diffuse (580 – 890 K), for different heating rates. Evidently all curves are very nearly linear. This indicates that the kinetics of the first step in the reaction is consistent with a diffusion-controlled model, in agreement with the TEM observations. The diffusion activation energy can be determined from the slopes of the curves in Figure 5a and is estimated to be 0.47 ± 0.08 eV. Equation (1) can then be used to calculate the reaction enthalpy rate during the calorimetry scans. Figure 5b compares the model curves with the experimental data showing good overall agreement between both.

The activation energy for the crystallization process can be determined from a Kissinger plot[37] of the heating rate versus peak temperature. The results are shown in Figure 5c for samples with both bilayer periods. The results for the multilayers with the 8.3 nm bilayer period show a significant amount of scatter because the overlap of both peaks in the calorimetry traces makes it difficult to determine an accurate value of the peak temperature. The results for the multilayers with the 4.1 nm period are better and provide an estimate of the activation energy of 2.4 eV. Although it is not possible to get an accurate value of the activation energy from the data points for the 8.3 nm samples, the results are certainly consistent with an activation energy of 2.4 eV.

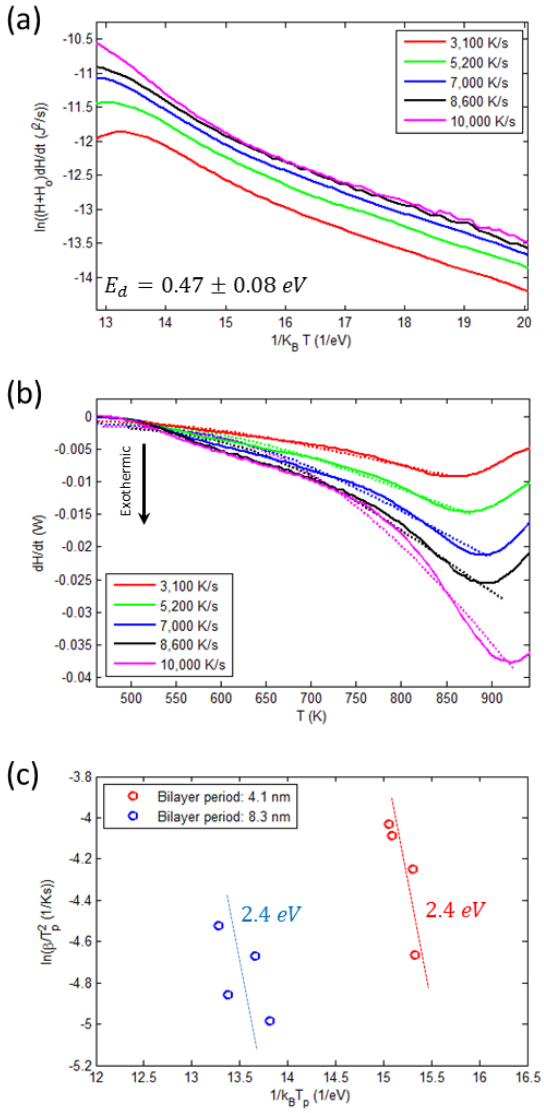

Figure 5. Kinetic analysis on the reaction in Zr/B multilayer: (a) $\ln\left(H+Ho\right)dHdt$ versus kBT for the temperature range of 580 ~ 890 K. Slopes in this plot is the activation energy of the diffusion process. (b) Reaction enthalpy rate as a function of temperature: model curves (dotted lines) with experimental curves (solid lines). Plots in (a-b) were generated from the nano-calorimetry measurements performed on the samples with a bilayer period of 8.3 nm. (c) Kissinger plots for crystallization peaks from the measurements on both 4.1 and 8.3 nm period samples

It is instructive to compare the measured activation energies to values reported in the literature. For instance, Samsonov et al reported an activation energy of 1.69 - 1.99 eV[38] for the diffusion of B in Zr, a value that is much higher than the diffusion activation energy found in this study. The activation energy obtained by Samsonov et al was

determined by measuring the thickness of ZrB_2 in Zr/B diffusion couples exposed to temperatures in excess of 1,373 K. No amorphous Zr/B phase was observed in their experiments. Formation of ZrB_2 thus required B to diffuse through crystalline ZrB_2, a process that is evidently much more difficult than diffusion through an amorphous phase, given the high activation energy. In fact, the activation energy measured by Samsonov et al is close to the activation energy for crystallization measured in this study. The crystallization activation energy is also close to the 2.57 eV activation energy reported for sintering of ZrB_2[39]. To the best of our knowledge, formation of an amorphous Zr/B alloy through inter-diffusion of B and Zr, and the very low associated activation energy have not been reported before. The phenomenon is similar, however, to the formation of amorphous phases during isothermal anneals in multilayers that contain components with a large negative Gibbs free energy of mixing and a large mismatch in atomic volume such as Au/La, Ti/Ni, and Ni/Zr[40, 41]. In these systems, diffusion through the amorphous reaction product is rate controlling, although the activation energies tend to be larger than the value reported here. We attribute this to the fact that the mismatch in atomic volumes in these systems is significantly smaller than in the Zr/B system.

It is possible to synthesize ZrB_2 directly from Zr and B powders using a self-propagating reaction. Even though this process is cost-effective, it has been regarded as a less-than-ideal technique to produce bulk ZrB_2[42]. The rapid heating rate (3,000 - 4,000K/s [42, 43]) associated with the process results in incomplete reaction of Zr and B, and in the formation of non-equilibrium phases[42]. Similar observations were made in our previous work on reactive multilayer where impurities in Zr arising from the deposition process prevented complete reaction between B and Zr[21]. Here we demonstrate that complete

reaction is possible as long as the impurity level is sufficiently low, and that this reaction occurs at relatively low temperatures. Thus, it may be possible to manufacture low-cost bulk ZrB_2 using self-propagating high-temperature synthesis (SHS), although attaining the requisite purity levels may be difficult using powders because of the native oxide on Zr and the affinity of Zr for hydrogen and other impurities. It may also be possible to use Zr/B reactive multilayers to braze ultra high-temperature materials. The Zr/B reaction is highly exothermic and a nano-structured Zr/B multilayer could be used as a local heat source to melt the brazing material. In a similar application, Ni/Al reactive multilayers have been utilized to braze silicon, bulk metallic glasses, and other alloys[44].

CONCLUSION

In conclusion, we have investigated the reaction kinetics of Zr/B multilayers using high-temperature nano-calorimetry combined with TEM. The multilayer reaction produces strongly textured ZrB_2 coatings below 1,300 K at heating rates ranging from 3,000 K/s to 10,000K/s. The Zr/B reaction proceeds in two stages: (1) inter-diffusion between the nano-crystalline Zr and the amorphous B layers and the formation of an amorphous Zr/B alloy, and (2) crystallization of the amorphous alloy to form crystalline ZrB_2. The formation of the amorphous alloy is diffusion limited and has a low activation energy of 0.47 eV. The crystallization step, in contrast, has a much higher activation energy of 2.4 eV. We believe that the kinetic information obtained in this study will provide useful insights into the synthesis of ZrB_2 using both conventional processing techniques and Zr/B reactive multilayers.

Supporting Information Available:

The Supporting Information includes the fabrication procedure of the PnSC device and the derivation of the kinetic model of the inter-diffusion in Zr/B multilayers. This material is available free of charge via the Internet at http://pubs.acs.org.

ACKNOWLEDGEMENTS

This work was supported by the Air Force Office of Scientific Research under Grant No. FA9550-12-1-0098. It was performed in part at the Center for Nanoscale Systems at Harvard University, which is supported by the National Science Foundation under Award No. ECS-0335765, and at the Materials Research Science and Engineering Center at Harvard University, which is supported by the National Science Foundation under Award No. DMR-0820484.

REFERENCES

(1) Fahrenholtz, W. G.; Hilmas, G. E.; Talmy, I. G.; Zaykoski, J. A., Refractory Diborides of Zirconium and Hafnium. *J. Am. Ceram. Soc.* **2007,** *90* (5), 1347-1364.

(2) Guo, S. Q., Densification of ZrB2-based Composites and Their Mechanical and Physical Properties: A review. *J. Eur. Ceram. Soc.* **2009,** *29* (6), 995-1011.

(3) Upadhya, K.; Yang, J. M.; Hoffman, W. P., Materials for Ultrahigh Temperature Structural Applications. *Am. Ceram. Soc. Bull.* **1997,** *76* (12), 51-56.

(4) Zamora, V.; Ortiz, A. L.; Guiberteau, F.; Nygren, M., Spark-Plasma Sintering of ZrB2 Ultra-High-Temperature Ceramics at Lower Temperature via Nanoscale Crystal Refinement. *J. Eur. Ceram. Soc.* **2012,** *32* (10), 2529-2536.

(5) Fahrenholtz, W. G.; Hilmas, G. E.; Zhang, S. C.; Zhu, S., Pressureless Sintering of Zirconium Diboride: Particle Size and Additive Effects. *J. Am. Ceram. Soc.* **2008,** *91* (5), 1398-1404.

(6) Fahrenholtz, W. G.; Hilmas, G. E.; Chamberlain, A. L.; Zimmermann, J. W., Processing and Characterization of ZrB2-based Ultra-high Temperature Monolithic and Fibrous Monolithic Ceramics. *J. Mater. Sci.* **2004,** *39* (19), 5951-5957.

(7) Sciti, D.; Guicciardi, S.; Bellosi, A.; Pezzotti, G., Properties of a Pressureless-Sintered ZrB2-MoSi2 Ceramic Composite. *J. Am. Ceram. Soc.* **2006,** *89* (7), 2320-2322.

(8) Silvestroni, L.; Sciti, D., Effects of MoSi2 Additions on The Properties of Hf- and Zr-B_2 Composites Produced by Pressureless Sintering. *Scripta Mater.* **2007,** *57* (2), 165-168.

(9) Zhang, S. C.; Hilmas, G. E.; Fahrenholtz, W. G., Pressureless Densification of Zirconium Diboride with Boron Carbide Additions. *J. Am. Ceram. Soc.* **2006,** *89* (5), 1544-1550.

(10) Thompson, M.; Fahrenholtz, W. G.; Hilmas, G., Effect of Starting Particle Size and Oxygen Content on Densification of ZrB2. *J. Am. Ceram. Soc.* **2011,** *94* (2), 429-435.

(11) Zamora, V.; Ortiz, A. L.; Guiberteau, F.; Nygren, M., Crystal-Size Dependence of the Spark-Plasma-Sintering Kinetics of ZrB_2 Ultra-High-Temperature Ceramics. *J. Eur. Ceram. Soc.* **2012,** *32* (2), 271-276.

(12) Spaepen, F.; Thompson, C. V., Calorimetric Studies of Reactions in Thin-Films and Multilayers. *Appl. Surf. Sci.* **1989,** *38* (1-4), 1-12.

(13) Michaelsen, C.; Barmak, K.; Weihs, T. P., Investigating the Thermodynamics and Kinetics of Thin Film Reactions by Differential Scanning Calorimetry. *J. Phys. D. Appl. Phys.* **1997,** *30* (23), 3167-3186.

(14) Highmore, R. J.; Somekh, R. E.; Evetts, J. E.; Greer, A. L., Differential Scanning Calorimetry Studies of Solid-State Amorphization in Multilayer Ni/Zr. *J. Less-Common Met.* **1988,** *140*, 353-360.

(15) Highmore, R. J.; Evetts, J. E.; Greer, A. L.; Somekh, R. E., Differential Scanning Calorimetry Study of Solid-State Amorphization in Multilayer Thin-Film Ni/Zr. *Appl. Phys. Lett.* **1987,** *50* (10), 566-568.

(16) Cotts, E. J.; Meng, W. J.; Johnson, W. L., Calorimetric Study of Amorphization in Planar, Binary, Multilayer, Thin-Film Diffusion Couples of Ni and Zr. *Phys. Rev. Lett.* **1986,** *57* (18), 2295-2298.

(17) Coffey, K. R.; Clevenger, L. A.; Barmak, K.; Rudman, D. A.; Thompson, C. V., Experimental-Evidence for Nucleation during Thin-Film Reactions. *Appl. Phys. Lett.* **1989,** *55* (9), 852-854.

(18) Clevenger, L. A.; Thompson, C. V., Nucleation-Limited Phase Selection during Reactions in Nickel Amorphous-Silicon Multilayer Thin-Films. *J. Appl. Phys.* **1990,** *67* (3), 1325-1333.

(19) Ma, E.; Thompson, C. V.; Clevenger, L. A., Nucleation and Growth during Reactions in Multilayer Al/Ni Films - the Early Stage of Al3 Ni Formation. *J Appl Phys* **1991,** *69* (4), 2211-2218.
(20) Weihs, T. P.; Barbee, T. W.; Wall, M. A., A Low-Temperature Technique for Measuring Enthalpies of Formation. *J. Mater. Res.* **1996,** *11* (6), 1403-1409.
(21) Lee, D.; Sim, G. D.; Xiao, K. C.; Choi, Y. S.; Vlassak, J. J., Scanning AC Nanocalorimetry Study of Zr/B Reactive Multilayers. *J. Appl. Phys.* **2013,** *114* (21).
(22) Swaminathan, P.; Grapes, M. D.; Woll, K.; Barron, S. C.; LaVan, D. A.; Weihs, T. P., Studying Exothermic Reactions in the Ni-Al System at Rapid Heating Rates Using a Nanocalorimeter. *J. Appl. Phys.* **2013,** *113* (14).
(23) Kummamuru, R. K.; De La Rama, L.; Hu, L.; Vaudin, M. D.; Efremov, M. Y.; Green, M. L.; LaVan, D. A.; Allen, L. H., Measurement of Heat Capacity and Enthalpy of Formation of Nickel Silicide Using Nanocalorimetry. *Appl. Phys. Lett.* **2009,** *95* (18).
(24) Cook, L. P.; Cavicchi, R. E.; Bassim, N.; Eustis, S.; Wong-Ng, W.; Levin, I.; Kattner, U. R.; Campbell, C. E.; Montgomery, C. B.; Egelhoff, W. F.; Vaudin, M. D., Enhanced Mass Transport in Ultrarapidly Heated Ni/Si Thin-Film Multilayers. *J. Appl. Phys.* **2009,** *106* (10).
(25) McCluskey, P. J.; Vlassak, J. J., Nano-Thermal Transport Array: An Instrument for Combinatorial Measurements of Heat Transfer in Nanoscale Films. *Thin Solid Films* **2010,** *518* (23), 7093-7106.
(26) Gregoire, J. M.; McCluskey, P. J.; Dale, D.; Ding, S. Y.; Schroers, J.; Vlassak, J. J., Combining Combinatorial Nanocalorimetry and X-ray Diffraction Techniques to Study the Effects of Composition and Quench Rate on Au-Cu-Si Metallic Glasses. *Scripta Mater.* **2012,** *66* (3-4), 178-181.
(27) Orava, J.; Greer, A. L.; Gholipour, B.; Hewak, D. W.; Smith, C. E., Characterization of Supercooled Liquid Ge2Sb2Te5 and Its Crystallization by Ultrafast-Heating Calorimetry. *Nat. Mater.* **2012,** *11* (4), 279-283.
(28) Xiao, K. C.; Gregoire, J. M.; McCluskey, P. J.; Vlassak, J. J., A Scanning AC Calorimetry Technique for the Analysis of Nano-Scale Quantities of Materials. *Rev. Sci. Instrum.* **2012,** *83* (11).
(29) Molina-Ruiz, M.; Lopeandia, A. F.; Gonzalez-Silveira, M.; Anahory, Y.; Guihard, M.; Garcia, G.; Clavaguera-Mora, M. T.; Schiettekatte, F.; Rodriguez-Viejo, J., Formation of Pd2Si on Single-Crystalline Si (100) at Ultrafast Heating Rates: An In-Situ Analysis by Nanocalorimetry. *Appl. Phys. Lett.* **2013,** *102* (14).
(30) Cebe, P.; Hu, X.; Kaplan, D. L.; Zhuravlev, E.; Wurm, A.; Arbeiter, D.; Schick, C., Beating the Heat - Fast Scanning Melts Silk Beta Sheet Crystals. *Sci. Rep.* **2013,** *3*.
(31) Ahrenberg, M.; Brinckmann, M.; Schmelzer, J. W. P.; Beck, M.; Schmidt, C.; Kessler, O.; Kragl, U.; Verevkin, S. P.; Schick, C., Determination of Volatility of Ionic Liquids at the Nanoscale by Means of Ultra-Fast Scanning Calorimetry. *Phys. Chem. Chem. Phys.* **2014,** *16* (7), 2971-2980.
(32) McCluskey, P. J.; Vlassak, J. J., Combinatorial Nanocalorimetry. *J. Mater. Res.* **2010,** *25* (11), 2086-2100.
(33) Golovanenko, S. A.; Natapova, A. B.; Klypin, B. A.; Kesaev, T. M., Recrystallization of Tungsten Alloys. *Met. Sci. Heat. Treat.* **1976,** *18* (9-10), 810-812.
(34) Xiao, K. C.; Gregoire, J. M.; McCluskey, P. J.; Dale, D.; Vlassak, J. J., Scanning AC Nanocalorimetry Combined with In-Situ X-ray Diffraction. *J. Appl. Phys.* **2013,** *113* (24).
(35) Huber, E. J.; Head, E. L.; Holley, C. E., The Heats of Formation of Zirconium Diboride and Dioxide. *J.Phys. Chem.* **1964,** *68*, 3040-3042.
(36) Vajeeston, P.; Ravindran, P.; Ravi, C.; Asokamani, R., Electronic Structure, Bonding, and Ground-State Properties of AlB2-Type Transition-Metal Diborides. *Phys. Rev. B.* **2001,** *63* (4).

(37) Kissinger, H. E., Reaction Kinetics in Differential Thermal Analysis. *Anal. Chem.* **1957,** *29* (11), 1702-1706.
(38) Samsonov, G. V.; Zhunkovskii, G. L., Mechanism of the Reaction of Refractory Metals with Boron in Vacuum Boriding. *Sov. Powder. Metall.* **1970,** *9*, 472-478.
(39) Pathak, S. K. M.; Das, S.; Das, S. K.; Ramachandrarao, P., Sintering Studies on Ultrafine ZrB_2 Powder Produced by a Self-Propagating High-Temperature Synthesis Process. *J. Mater. Res.* **2000,** *15* (11), 2499-2504.
(40) Schwarz, R. B.; Johnson, W. L., Formation of an Amorphous Alloy by Solid-State Reaction of the Pure Polycrystalline Metals. *Phys. Rev. Lett.* **1983,** *51* (5), 415-418.
(41) Clemens, B. M., Solid-State Reaction and Structure in Compositionally Modulated Zirconium-Nickel and Titanium-Nickel Films. *Phys. Rev. B.* **1986,** *33* (11), 7615-7624.
(42) Chamberlain, A. L.; Fahrenholtz, W. G.; Hilmas, G. E., Low-Temperature Densification of Zirconium Diboride Ceramics by Reactive Hot Pressing. *J. Am. Ceram. Soc.* **2006,** *89* (12), 3638-3645.
(43) Mishra, S. K.; Das, S.; Pathak, L. C., Defect Structures in Zirconium Diboride Powder Prepared by Self-Propagating High-Temperature Cynthesis. *Mat. Sci. Eng. A.* **2004,** *364* (1-2), 249-255.
(44) Wang, J.; Besnoin, E.; Duckham, A.; Spey, S. J.; Reiss, M. E.; Knio, O. M.; Powers, M.; Whitener, M.; Weihs, T. P., Room-Temperature Soldering with Nanostructured Foils. *Appl. Phys. Lett.* **2003,** *83* (19), 3987-3989.

Supporting Information

Low-Temperature Synthesis of Ultra High-Temperature Coatings of ZrB_2 Using Reactive Multilayers

Dongwoo Lee, Gi-Dong Sim, Kechao Xiao, and Joost J. Vlassak*

School of Engineering and Applied Sciences, Harvard University, Cambridge, Massachusetts 02138, United States

*e-mail: vlassak@seas.harvard.edu

Fabrication of PnSC device

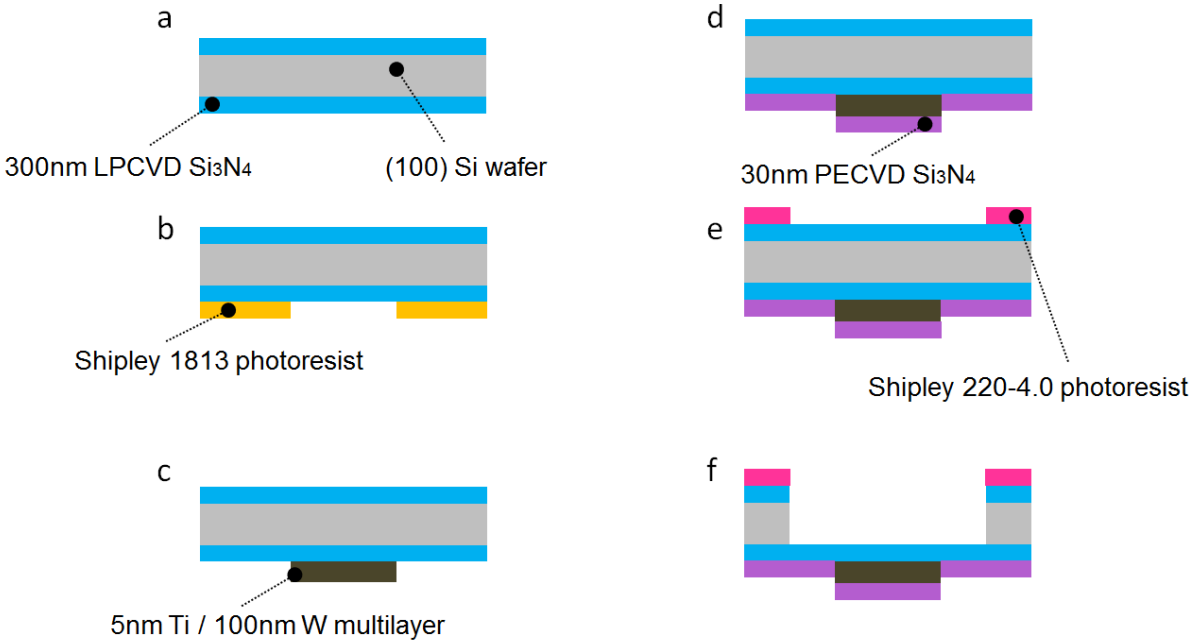

Figure S1. (a) The fabrication process starts with a 55mm × 55mm × 200 μm (100) Si wafer passivated with 300 nm low-stress LPCVD nitiride (WRS Materials). (b) Photoresist (Shipley 1813) is then spin coated and patterend on the front side of the wafer. (c) Then 5 nm titanium and 100 nm tungsten are magnetron sputter deposited. The metal layers are defined using a lift-off procedure. Titanium is deposited to improve adhesion between tungsten and nitride and to form a Ti/W alloy that has a higher recrystallization temperature, compared to pure tungsten. Copper is then patterned using the same procedure (not shown in the figure) to connect the heater to the contact pads. (d) After the metal patterning, 30 nm Si_3N_4 is coated on the front side to protect the metal layers from oxidation. (e) To make freestanding membranes, photoresist (Shipley 220-4.0) is patterned on the backside and (f) Si is removed using a SPTS Rapier DRIE system.

Derivation of the Kinetic Model of Inter-diffusion

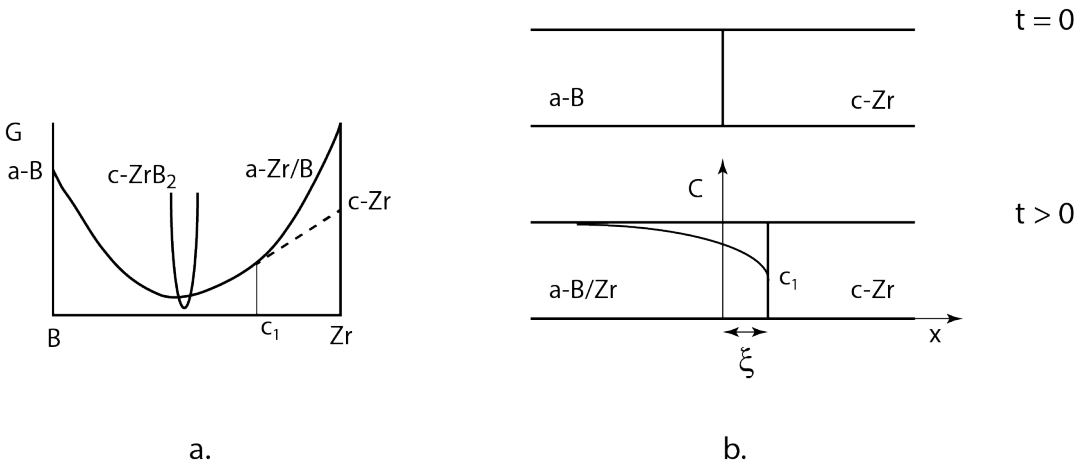

Figure S2. (a) Schematic free energy diagram for the B/Zr system. Crystalline Zr is in meta-stable equilibrium with an amorphous phase with B concentration C_1. (b) Concentration profiles after inter-diffusion.

Figure S2 shows a simple model for the inter-diffusion of amorphous B and crystalline Zr: c-Zr is in meta-stable equilibrium with an amorphous B/Zr phase with B concentration C_1; the solid solubility of B in c-Zr is taken negligibly small (a). After inter-diffusion, the phase boundary has shifted a distance ξ and the B concentration in the amorphous phase has become non-uniform (b). We only consider the initial stage of the process where the diffusion distance is much smaller than the bilayer period of the sample. This problem can be formulated as a moving-boundary problem of the Stefan type[1]. The concentration profile is the solution of the Fick's diffusion equation with the following boundary conditions,

$$\begin{aligned} C(-\infty,t) &= 1, \\ C(\xi,t) &= C_1. \end{aligned} \tag{S1}$$

The mass balance at the interface between the amorphous and crystalline phases further requires that

$$\frac{d\xi}{dt} = -\frac{D}{C_1}\frac{dC}{dx}\bigg|_{\xi}. \tag{S2}$$

Under isothermal conditions, the solution of this problem is a variant of Neumann's similarity solution and is given by

$$C(x,t) = 1 - \frac{1-C1}{1+\mathrm{erf}\,\alpha}\left(1+\mathrm{erf}\left(\frac{x}{2\sqrt{Dt}}\right)\right), \tag{S3}$$

$$\xi = 2\alpha\sqrt{Dt}\,, \tag{S4}$$

where D is the inter-diffusion coefficient and α is a function of C_1, defined implicitly by

$$\alpha\left(1+\mathrm{erf}\,\alpha\right)\exp\alpha^2 = \frac{1-C1}{\sqrt{\pi}C1}\,. \tag{S5}$$

Taking the enthalpy released during inter-diffusion to be proportional to the Zr concentration in the amorphous phase, it follows that

$$H = \frac{\Delta H}{t_{Zr}}\int_{-\infty}^{\xi}\left(1-C\right)dx = 2\frac{\alpha\Delta H}{t_{Zr}}\sqrt{Dt}\,, \tag{S6}$$

so that

$$H\frac{dH}{dt} = 2\left(\frac{\alpha\Delta H}{t_{Zr}}\right)^2 D\,. \tag{S7}$$

In this expression ΔH is the total enthalpy released during inter-diffusion of a single bilayer and t_{Zr} is the thickness of the Zr layers. Equation (S7) can be used to determine the diffusion coefficient from the reaction enthalpy rate obtained in an experiment performed under isothermal conditions. If experiments are not conducted under isothermal conditions, the solution to the diffusion problem is still valid, provided the product Dt is replaced by a quantity that depends on the entire temperature history $T(t)$ of the sample,

$$\tau = \int_{0}^{t} D\left(T\left(t\right)\right)dt\,. \tag{S8}$$

For an experiment performed at constant heating rate β, Eq. (S6) then becomes

$$H = 2\frac{\alpha\Delta H}{t_{Zr}\sqrt{\beta}}\sqrt{\int_{T_o}^{T} D\left(T\right)dT}\,, \tag{S9}$$

but the product $H\frac{dH}{dt}$ is still given by Eq. (S7) despite the non-isothermal conditions. If the diffusion coefficient D can be described by an Arrhenius equation, it follows that

$$\ln\left(H\frac{dH}{dt}\right) = 2\ln\left(\frac{\alpha\Delta H\sqrt{2D_o}}{t_{Zr}}\right) - \frac{E_d}{k_B T}\,, \tag{S10}$$

where k_B is the Boltzmann constant, E_d is the diffusion activation energy, and D_o is the pre-exponential factor of the diffusion coefficient. If some intermixing has taken place during deposition of the reactive multilayer, Eq. (S10) may need to be replaced by

$$\ln\left(\left(H+H_o\right)\frac{dH}{dt}\right)=2\ln\left(\frac{\alpha\Delta H\sqrt{2D_o}}{t_{Zr}}\right)-\frac{E_d}{k_BT}, \tag{S11}$$

where H_o is the enthalpy associated with the intermixing. A graph of $\ln(H+Ho)dH/dt$ versus $1/k_BT$ produces a straight line with as slope the activation energy Ed.

1. Crank, John. *Free and Moving Boundary Problems*. Clarendon press Oxford, 1984.